This document is complies with the paper:

Simone Sirianoa, Alessandro Tassone, Gianfranco Caruso, Alessandro Del Nevo, "MHD forced convection flow in dielectric and electro-conductive rectangular annuli", Fusion Engineering and Design 159 (2020) 111773, Fusion Engineering and Design, https://doi.org/10.1016/j.fusengdes.2020.111773

MHD forced convection flow in dielectric and electro-conductive rectangular annuli

Simone Siriano[a*], Alessandro Tassone[a], Gianfranco Caruso[a], Alessandro Del Nevo[b]

[a]*Department of Astronautical, Electrical and Energy Engineering, Sapienza University of Rome, Rome, Italy*
[b]*ENEA FSN-ING-PAN, ENEA CR Brasimone, Camugnano, Italy*

The Breeding Blanket is a fundamental component of a nuclear fusion reactor and the Water-Cooled Lead Lithium (WCLL) blanket is one of the possible solutions proposed. In this concept, liquid lithium-lead eutectic alloy (PbLi) serves as tritium breeder, tritium carrier and neutron multiplier. The liquid metal is distributed within the breeding zone by two co-axial rectangular channels and, interacting with the reactor magnetic field, leads to the arising of MagnetoHydroDynamic (MHD) effects. In this work, the general-purpose CFD code Ansys CFX 18.2 is used to study this uncommon configuration, modelled as a prototypical square annular channel. The study covers a wide range of magnetic field intensity (up to $Ha = 2000$) and two values for the wall conductance ratio ($c_w = 0$ and $c_w = 0.1$) representing, respectively, the ideal insulated case and one more closely approaching the WCLL manifold actual conditions. For both these scenarios, characteristic flow features and their evolution with increasing magnetic field are discussed. A correlation is found linking the pressure loss in the studied configuration and an equivalent square channel through a corrective factor ε, which exhibits an asymptotic behavior for $Ha > 1000$ equal to $\varepsilon_{c_w=0} \cong 2.44$ and $\varepsilon_{c_w=0.1} \cong 1.12$.

Keywords: blanket engineering, DEMO, Magnetohydrodynamic (MHD), manifold, PbLi, WCLL

1. Introduction

One of the key components of a nuclear fusion reactor is the Breeding Blanket (BB) that, surrounding the plasma chamber, fulfills the tasks of tritium breeding and thermal power extraction for electricity production. In the Water-Cooled Lead Lithium (WCLL) blanket, Eurofer is employed as structural material, PbLi serves as tritium breeder and carrier and neutron multiplier, whereas pressurized water cools the system. The current design (2018), based on DEMO 2017 specifications and derived from R&D activities conducted in the framework of the EUROfusion Programme, relies on the Single Module Segment approach, with a breeding element repeated along the poloidal direction (Fig. 1A) [1]. The liquid metal is distributed to the elementary cells composing the Breeding Zone (BZ) through a compact poloidal manifold, which fulfills both the distribution and collection task. The manifold is composed by two long co-axial rectangular channels, in which the external one, tasked with distributing the liquid metal, can be described as a rectangular annular duct (Fig. 1B).

The motion of liquid metal, exposed to the reactor magnetic field, induces electric currents. In turn, these interact with the magnetic field and generate a Lorentz force that leads to the appearance of MagnetoHydroDynamic (MHD) effects, which significantly influence the flow features. The Lorentz force is not uniformly distributed on the channel cross-section but is rather dependent on the overall magnitude and paths of the current inside the fluid, which, in turn, depends on the electric conductivity of the walls.

The first studies on MHD flow in a circular gap are probably the work by Todd [2] for an insulated case and

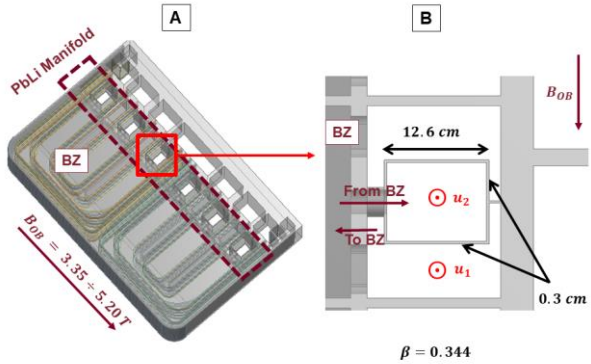

Fig. 1. WCLL2018 outboard breeding blanket configuration at the equatorial plane (A) and PbLi manifold co-axial channel detail without water tubes (B).

the work by Kumamaru [3] for an electro-conductive case.

The most recent works are limited to industrial studies and the first one of fusion interest is probably the work by Buhler [4]. Some numerical studies have already been reported for a MHD flows in annular channels. Buhler et al. [5] consider MHD pressure-driven and magneto-convective motion within the gap described by an external square channel and an internal cylindrical pipe, both electrically insulated. Studies dealing with conductive walls are relatively scarce for this configuration. One of the few examples of note is Chen et al. [6] that investigates the MHD phenomena in an assembly composed by three co-axial rectangular channels electrically decoupled by each other through multi-layer flow channel inserts of arbitrary conductivity.

In this paper, the MHD forced convection flow in a co-axial annular configuration is studied. Numerical simulations are performed for a wide range of magnetic

field intensity ($Ha = 10 \div 2000$) using the general CFD code ANSYS CFX 18.2 and, at first, the analysis is focused on an ideal case in which both the external and internal annulus walls are perfectly insulating, in order to characterize the basic flow features and phenomena. Successively, the study is extended to a more realistic case, such as it is foreseen in the WCLL current design, where both walls are characterized by finite electrical conductivity.

A correct estimate of the MHD pressure drop is critical to design the WCLL PbLi loop, therefore an accurate estimate for this configuration is required. The pressure gradient calculated by the CFD code, for both dielectric and electro-conducting annuli (∇p_a), is compared with the analytical value characterizing the fully developed flow in an equivalent channel (∇p_c) to define proper engineering correction factors ($\varepsilon = \nabla p_a / \nabla p_c$) to correlate them and allow for results extrapolation at higher field intensity.

2. Numerical model

The geometry of the WCLL 2018 design manifold external channel is quite complex featuring several conductive obstacles, an asymmetric layout and electromagnetic coupling with the internal channel (Fig. 1B). To characterize the flow features and phenomena in this uncommon configuration, the manifold external channel is simplified to its more basic analogue: a square annular channel with the same internal width and blockage ratio β (Fig. 2A) with respect to the original channel. The internal manifold channel is not modeled, thus neglecting coupling phenomena, and obstacles are removed to streamline the configuration. The resulting equivalent model is shown in Fig. 2A and its geometrical parameters are collected in Table 1.

An isothermal, steady and fully developed flow of liquid PbLi, which physical properties are reported in Table 2, flows along the z-direction through a uniform and steady magnetic field $\boldsymbol{B}$ parallel to the x-direction.

2.1 Governing equations and dimensionless groups

The MHD governing equations in ANSYS CFX 18.2 are implemented introducing a body force source term in the momentum equation (Lorentz force) and additional equations for the electric potential φ and current density $\boldsymbol{j}$ (Ohm's Law) [7]. Under the assumptions considered in this work, the inductionless approximation is applicable and, therefore, the dimensionless governing equations used by the code are expressed as [7] [8]

$$\frac{1}{N}\left[\frac{\partial \boldsymbol{u}}{\partial t} + (\boldsymbol{u}\cdot\nabla)\boldsymbol{u}\right] = -\nabla p + \frac{1}{Ha^2}\nabla^2\boldsymbol{u} + \boldsymbol{j}\times\boldsymbol{B} \qquad (1)$$

$$\boldsymbol{j} = -\nabla\varphi + \boldsymbol{u}\times\boldsymbol{B} \qquad (2)$$

$$\nabla^2\varphi = \nabla\cdot(\boldsymbol{u}\times\boldsymbol{B}) \qquad (3)$$

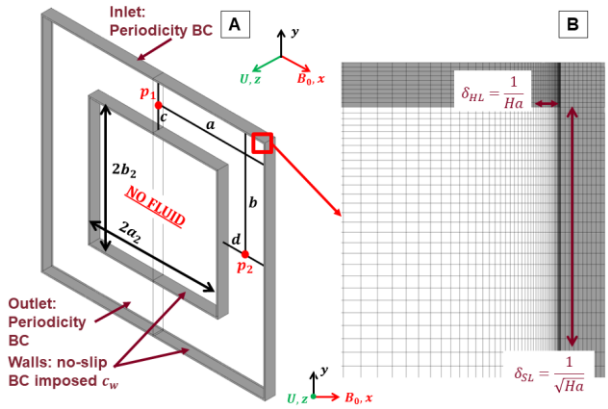

Fig. 2. Computational domain with BCs, velocity profile sampling locations (a, b, c, d) and velocity probing points (p_1, p_2) for mesh sensitivity study (A). Mesh detail (B).

Table 1. Geometrical parameters of annular channel.

Parameter	Symbol	Value (unit)
Aspect ratio	$a/b = a_2/b_2$	1
Blockage ratio	β	0.344
External side	$2a$	21.47 (cm)
Internal side	$2a_2$	12.60 (cm)
Internal gap	$c = d$	4.44 (cm)
Walls thickness	t_w	0.30 (cm)

Table 2. Material properties of PbLi at 600 K [9].

Property	Symbol	Value (unit)
Density	ρ	9806 (kg/m^3)
Viscosity	μ	$1.96 \cdot 10^{-3}$ $(Pa\ s)$
Electrical conductivity	σ	$8.75 \cdot 10^5$ (S/m)

Table 3. Dimensionless parameter for the WCLL 2018 conditions and simplified model.

Dim. Number	Symbol	WCLL	Model
Reynolds	Re	$\cong 5000$	1
Hartmann	Ha	$\cong 9000$	$10 \div 2000$
Stuart	N	$\gg 1$	$\gg 1$

where p is the pressure, u the velocity field and L_c the characteristic length, that is the half-width of the external side (Table 1).

The interaction parameter $N = \sigma L_c B^2/\rho u_0$ gives the ratio of the electromagnetic forces to the inertia forces, the Hartmann number $Ha = L_c B^2\sqrt{\sigma/\mu}$ represents the ratio of the electromagnetic forces to the viscous forces and characterizes the boundary layer thickness. u_0 is the mean velocity that it's set to give a Reynolds number equal to 1, so we assume that the flows remain laminar ($N >> 1$) and depends only on Ha. Table 3 shows the dimensionless numbers in the WCLL2018 and those considered in this work. Manifold MHD flow is expected to be inertialess, and this condition is maintained at low Ha by proper scaling of the model main velocity. At the walls perpendicular to $\boldsymbol{B}$ (Hartmann walls) the boundary layers (Hartmann layer, HL) width is $\delta_H = L_c/Ha$, at the walls parallel to $\boldsymbol{B}$ (side walls) the boundary layer (side layer, SL) width is $\delta_S = L_c/\sqrt{Ha}$.

The influence of the electrical conductivity of the walls is represented by the conductance ratio $c_w = (\sigma_w\, t_w)/(\sigma L_c)$, where σ_w and t_w are, respectively, the wall conductivity and thickness. This parameter is assumed uniform in the model, whereas the opposite case is more commonly encountered in practice, as shown in Fig. 1B.

2.2 Boundary conditions and discretization scheme

The simulations were performed with the "high resolution" advection scheme. The mesh adopted is non-uniform, structured and composed by hexahedral elements, which are stretched to provide a finer resolution near the walls to resolve the boundary layers (Fig. 2B). All the simulations have been initialized with the respective hydrodynamic solutions to facilitate convergence.

Fig. 2A shows the boundary conditions (BCs). No-slip ($\boldsymbol{u} = \boldsymbol{0}$) is used for all the walls whereas, to represent a fully-developed flow, translation periodicity with fixed flow rate ($\Gamma_i = \Gamma_o$) is established between the inlet and outlet surface, thus simulating an infinite length channel. Regarding the electromagnetic BCs, a wall conductivity equal to zero is imposed for the insulated case ($c_w = 0$), whereas, for the electroconductive model, a uniform and finite conductivity is assumed ($c_w = 0.1$) for both internal and external walls. Eq. 3 is solved through the coupling of the solid (representing the duct walls) and fluid computational domain where, at the interface, is applied the "conservative interface flux" condition, which enforces current normal ($j_{n1} = j_{n2}$) and electric potential conservation ($\varphi = \varphi_w$) [10].

This assumption is not entirely realistic for the manifold external channel, where external walls are characterized by non-uniform thickness and the thin internal one will likely feature $c_w \ll 0.1$. Nevertheless, it was judged a suitable approximation to isolate the most important phenomena in the prototypical configuration studied.

2.3 Mesh sensitivity study

A mesh sensitivity study was performed for the perfectly insulated annulus at $Ha = 50$ to demonstrate the independence of the numerical results from grid resolution and to assess the Hartmann layer minimum refinement required. Since no analytical solutions are available for code validation, the velocity values at the probing point p_1 and p_2 showed in Fig. 2A, and the pressure gradient, are chosen as control parameters.

Table 4 shows the results, assuming 8 HL subdivisions as the reference case: at least 2 elements are required within the HL to obtain a convergent solution, whereas between 6 and 7 elements are necessary to achieve parameters independence from grid resolution. Therefore, a mesh with a subdivision of 7 elements in the Hartmann layer has been adopted for all the cases. In addition, CFX has been already validated for an MHD pressure-driven flow in a simpler configuration (rectangular channel) up to $Ha = 1.5 \cdot 10^4$ for both insulated and electro-conductive walls [11] [12].

Table 4. Results of mesh sensitivity study, errors related to the 8 HL subdivisions case.

HL sub.	Pressure gradient Error [%]	Velocity at p_1 Error [%]	Velocity at p_2 Error [%]	Mesh elements
0	N.C	N.C	N.C	9954
1	N. C	N.C	N.C	18480
2	1.85	0.66	0.91	26520
3	0.91	0.15	0.55	33288
4	0.54	0.40	0.37	40320
5	0.16	0.14	0.20	49128
6	0.02	0.9	0.13	58200
7	≈ 0	0.22	0.02	67392
8	0.00	0.00	0.00	72576

This model seems to show a remarkable difference in its numerical stability depending on the wall conductivity. For the insulated case, a first model was created adopting a "zero flux" BC, which enforces $\partial\varphi/\partial n = 0$ and allows to not include the walls in the computational domain, thus saving mesh elements and, in general, computational time. Conversely, this model proved to be numerical unstable and required very small element aspect ratio to achieve convergence, which greatly inflated the element count compared with an analogous conjugated model. For this reason, the walls have also been modelled for simulations including insulated walls.

3. Flow Features

3.1 Perfectly insulating cases: $c_w = 0$

Fig. 3 shows the velocity contour while Fig. 4 shows the dimensionless velocity distribution along four sampling locations, as shown in Fig. 2A: a, b, c and d. The velocity is scaled with the mean velocity u_0 whereas the lengths are the linear coordinate of the sampling lines which have the same direction of the respective axises. Since the flow is symmetrical with respect to $x = 0$, the results are shown on half of the channel.

An increase in Ha shows that the hydraulic flow develops in two uniform cores (Fig. 3A) connected by an internal layer (IL), a behavior also reported in the similar cases investigated by Buhler [5] and Chen [6]. A quicker slug flow develops in the two sub-channels parallel to $\boldsymbol{B}$, called Fast Core (FC), where the velocity reaches the uniform value of about $1.6\, u_o$ (Fig. 4A), whereas a slower slug flow appears in the channel region mostly perpendicular to $\boldsymbol{B}$, called Slow Core (SC), where the velocity reaches the uniform value of about $0.3\, u_o$ (Fig. 4C). Near the channel walls, both internal and external, classic Hartmann (Fig. 4A, C) and Shercliff layer are present (Fig. 4B, D).

Fig. 5 shows the topology of the electric currents for $Ha = 10$ and $Ha = 2000$. At low Ha, two currents loops are observed closing, respectively, through the internal (red line) and external wall Hartmann layer (blue line). These loops share almost equally the duct cross-section and converge toward two critical points, marked with diamonds, placed on the top and bottom external wall.

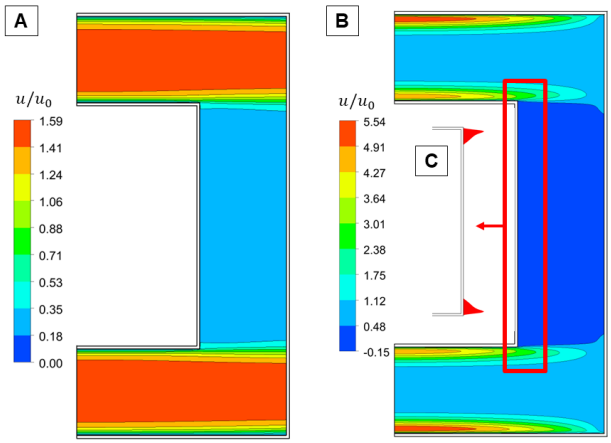

Fig. 3. Velocity contour for $Ha = 2000$ for $c_w = 0$ (A) and $c_w = 0.1$ (B). Counter flow zone locations (C).

However, not every current path cross both FC and SC regions and, in fact, some appear to be restricted to either one or the other forming tighter loops. This feature is particularly evident for the external path where shorter loops, marked by black line, are separated into two sub-circuits clustered around the external corners by a singularity point, marked with a cross, placed at duct mid-line.

When Ha is increased, the critical points move toward the internal wall corners and current loops accordingly rearrange: the internal loop becomes restricted to SC, whereas the other one is compressed toward the external Hartmann layer and, at the same time, stretched to occupy the whole FC. As a result, current lines belonging to this loop that are moving into FC becomes aligned to B within a thin band, called internal layer (IL), whereas those belonging to the shorter sub-circuits do not cross it and, therefore, are restricted to the FC region. This rearrangement appears to be responsible for the quick and fast slug flow development: shorter current path in SC offers higher resistance to the flow, whereas the contrary happens for the longer, stretched-out, FC current loop. The internal layer, similar in scale to the Shercliff one, is the boundary between the two cores and current loops, and, as result, is characterized by an intense velocity gradient. This behavior is quite similar to what observed by Buhler et al. [5] for a circular insulated annulus where, analogously, the internal layer separates two distinct core regions.

3.2 Electroconductive cases: $c_w = 0.1$

Considering an electro-conductive channel changes substantially the flow features, as shown in Fig. 6. At low Ha, the general flow is very similar to the insulating case but, even at $Ha = 10$, it is evident that the core region separation is already more pronounced, cfr. Fig. 4A and Fig. 4D with Fig. 6A and Fig. 6D. Further increasing Ha, two high velocity jets develop at channel walls aligned with the magnetic field (Fig. 3B and Fig. 6B): for $Ha = 2000$, the external jet has a velocity of about 5.5 u_o and the internal of about 4.9 u_o. The difference between the peak velocity is due to the weaker electric potential gradient at the internal wall.

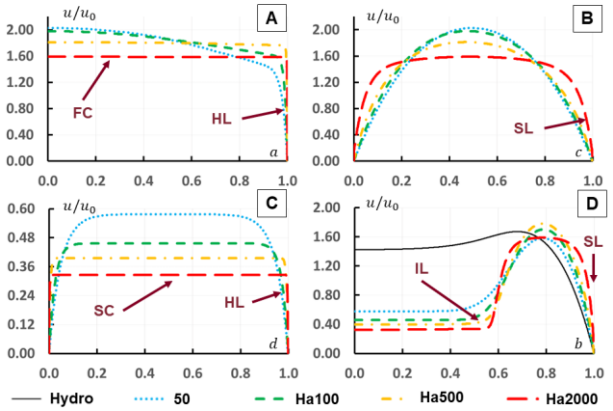

Fig. 4. Velocity distribution for $c_w = 0$ at a (A), c (B), d (C) and b (D).

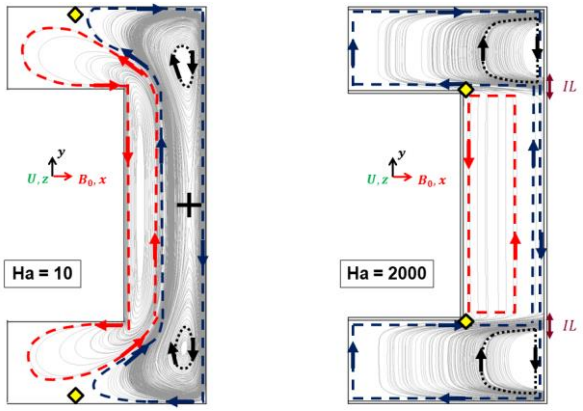

Fig. 5. Current streamlines for $c_w = 0$ at $Ha = 10$ and $Ha = 2000$ with critical point (diamonds) and singularity point (cross).

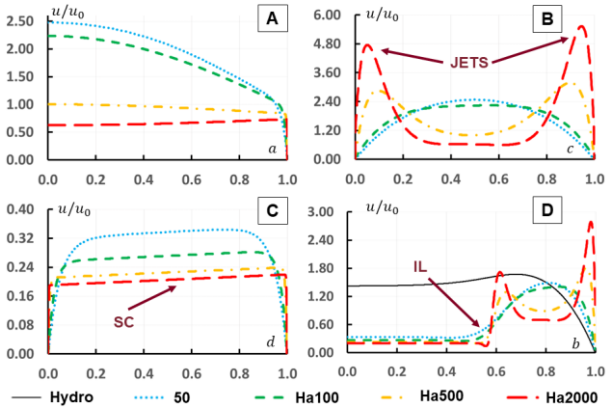

Fig. 6. Velocity distribution for $c_w = 0.1$ at a (A), c (B), d (C) and b (D).

Between these jets, the velocity is almost constant but, at 0.6 u_o, this core is significantly slower compared with the insulated case analogue. In SC, the flow is still more aggressively dampened (Fig. 6C) and the velocity is, again, lower than in FC, thus resulting in the internal layer formation. The internal jet propagates only partially in the internal layer where it matches with the core close to the external wall (Fig. 6D).

As expected, the currents flow preferentially through the conductive walls, that have a smaller electrical resistance with respect of the very thin boundary layers,

changing the topology of the electric current field with respect to the insulated case. Already at low Ha, the critical point (diamonds in Fig. 7) move into the top and bottom internal side wall, expanding the external current loop (blue line) to almost all the FC and, consequently, nearly confining the internal loop (red line) to the SC. Tighter loops, belonging to the main paths, but entirely restricted within either SC or FC (black line), are another features that is analogous to the insulated case.

When Ha is increased, the critical points move from the internal side wall to the internal Hartmann wall, further narrowing the internal loop to a smaller portion of the SC. Unlike the insulated case, the current lines passing from the SC to the FC are no longer aligned with $\boldsymbol{B}$ but, rather, are warped into a bow-like shape. Not all these currents pass through the internal side wall but, instead, a significant share directly crosses the IL into the FC just above the internal wall corner, thus forming shorter sub-circuits, which are marked in Fig. 7 with black line.

This current topology can probably explain the slope of the velocity distribution within SC (Fig. 6C): the shorter internal loop (red line) offers slightly higher resistance to the flow with respect to the longer external loop (blue line), therefore the velocity increases moving from the side internal wall to the side external wall.

It's important to note that, starting from $Ha > 500$, a counter flow zone begin to develop near the corner of the inner channel (Fig. 3C), probably due to the interaction between internal jet, IL, and SC. This region slowly increases in size and carried flow rate with Ha but, even if extrapolated to operative conditions, does not amount to more than 0.5% total flow rate.

4. Pressure drop analysis: correction factor ε

In order to estimate the MHD pressure drop in WCLL PbLi in-vessel loop, the pressure gradient calculated by the CFD code (∇p_a) for both dielectric and electro-conducting annuli is compared with the analytical value characterizing the fully developed flow in a dielectric [13] and electro-conducting [14] equivalent channel (∇p_c), defining the correction factors $\varepsilon = \nabla p_a / \nabla p_c$, which, in general, will assume a different value depending on the model geometrical parameters (e.g. aspect and blockage ratio).

The equivalent channel has the same aspect ratio $(a/b = 1)$ and characteristic length with respect of the annular channel modelled with CFX, with a consequently increased flow area. Choosing the mass flow rate as an imposed parameter, the mean velocity for that channel is smaller than the mean velocity of the annulus.

As shown in Fig. 8, for the perfectly insulated annulus the factor reaches a constant value of about $\varepsilon_{c_w=0} \cong 2.44$ for $Ha > 500$, whereas for the electro-conductive annulus reaches a constant value of about $\varepsilon_{c_w=0.1} \cong 1.12$ for $Ha > 1000$ (Fig. 9). From these results, it is conceivable to estimate the pressure gradient, and consequently the pressure drop, for a square annular channel for $Ha > 2000$ by calculating the pressure loss

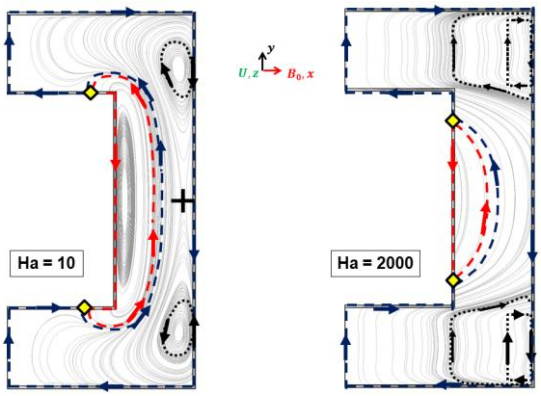

Fig. 7. Current streamlines for $c_w = 0.1$ at $Ha = 10$ and $Ha = 2000$ with critical point (diamonds) and singularity point (cross).

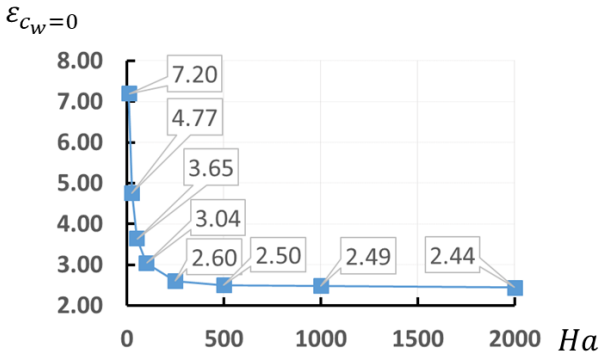

Fig. 8. Correction factor ε for dielectric annulus $c_w = 0$.

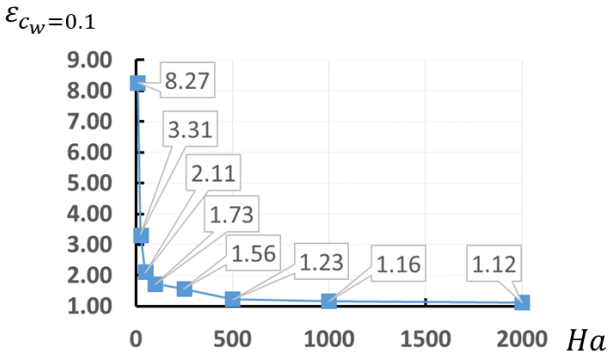

Fig. 9. Correction factor ε for conductive annulus $c_w = 0.1$.

in an equivalent square channel and multiplying it by the appropriate correction factor (δ_k) without the need to perform a numerical simulation. However, it should be noted that the corrective factors deduced from these calculations are strictly valid only for the chosen aspect and blockage ratio.

Considering the WCLL 2018 configuration, where it is expected an average magnetic field intensity $\overline{B} = 3.95\ T$, a mass flow rate for each annular channel of $2.73\ kg/s$, a characteristic length of $10.74\ cm$ and assuming a uniform conductance ratio $c = 0.1$ for the channel walls, the estimated MHD pressure gradient considering $\varepsilon_{w=0.1} = 1.12$ it's expected to be $7966\ Pa/m$ that, for the entire manifold lengths of $17\ m$, amounts to a pressure drop of $135.4\ kPa$. This is a rough estimate

of the pressure drop since it does not consider the additional losses due to obstacles and coupling. This technique is used to estimate the overall pressure drop for both the inboard and outboard PbLi manifold in Ref [15].

5. Conclusions and follow up

The MHD forced convection flow in dielectric and electro-conducting rectangular annuli is investigated with ANSYS CFX 18.2 code to a Hartmann number up to 2000. The perfectly insulated annulus ($c_w = 0$) shows the development of two well-defined cores with the increase of Ha: a fast core in the direction aligned with $\boldsymbol{B}$ and a slow core in the direction normal to $\boldsymbol{B}$. These cores match with the wall through the usual MHD boundary layers and match each other with an internal layer. With electro-conductive walls, the fast core is substituted by two intensive jets close to the walls, with a damped region between these and a more damped slow core compared with the insulated case.

The annular pressure gradient has been correlated with the pressure gradient of an equivalent square channel for which exist an analytical solution, developing a correction factor between the two configurations. This factor shows an asymptotical behavior for $Ha > 1000$, and allows to estimate the pressure drop for a similar configuration at higher Hartmann numbers without performing a numerical simulation.

This technique can provide only a rough estimate of the pressure drops because it is not considering the electrocoupling between the co-axial channel, that should be of fundamental importance for the pressure drop analysis. This phenomenon is studied in [16].

Follow up activities will be focused on extending the annular channel characterization to a more realistic configuration including non-unitary aspect ratio, offset of the internal channel and non-uniform wall conductance ratio. Heat transfer with the WCLL cooling system pipes, that cross the external channel, and the magneto-convective phenomena arising in the manifold will be treated in another paper.

Acknowledgments

This work has been carried out within the framework of the EUROfusion Consortium and has received funding from the Euratom research and training programme 2014-2018 and 2019-2020 under grant agreement No 633053. The views and opinions expressed herein do not necessarily reflect those of the European Commission.

References

[1] A. Del Nevo, P. Arena, G. Caruso, P. Chiovaro, P.A. Di Maio, M. Eboli, F. Edemetti, N. Forgione, R. Forte, A. Froio, F. Giannetti, G. Di Gironimo, K. Jiang, S. Liu, F. Moro, R. Mozzillo, L. Savoldi, A. Tarallo, M. Tarantino, A. Tassone, M. Utili, R. Villari, R. Zanino, E. Martelli, Recent progress in developing a feasible and integrated conceptual design of the WCLL BB in EUROfusion project, Fusion Eng. Des. 146 (2019) 1805–1809. https://doi.org/10.1016/j.fusengdes.2019.03.040.

[2] L. Todd, Hartmann flow in an annular channel, J. Fluid Mech. 28 (1967) 371–384. https://doi.org/10.1017/S0022112067002137.

[3] H. Kumamaru, Magnetic pressure drop and heat transfer of liquid metal flow in annular channel under transverse magnetic field, J. Nucl. Sci. Technol. 21 (1984) 393–400. https://doi.org/10.1080/18811248.1984.9731060.

[4] L. Bühler, Poloidal MHD flow in the European TAURO blanket concept, Karlsruhe, 1999. https://publikationen.bibliothek.kit.edu/270046437.

[5] L. Bühler, C. Mistrangelo, MHD flow and heat transfer in model geometries for WCLL blankets, Fusion Eng. Des. 124 (2017) 919–923. https://doi.org/10.1016/j.fusengdes.2017.01.014.

[6] H. Chen, T. Zhou, H. Zhang, Z. Meng, Numerical investigation of liquid metal magnetohydrodynamic flow in multilayer flow channel inserts, Fusion Eng. Des. 88 (2013) 2939–2944. https://doi.org/10.1016/j.fusengdes.2013.06.006.

[7] U. Müller, L. Bühler, Magnetofluiddynamics in Channels and Containers, I, Springer-Verlag Berlin Heidelberg, 2001. https://doi.org/10.1007/978-3-662-04405-6.

[8] ANSYS Inc., ANSYS CFX Solver Theory Guide 18.2, ANSYS, 2017.

[9] D. Martelli, A. Venturini, M. Utili, Literature review of lead-lithium thermophysical properties, Fusion Eng. Des. 138 (2019) 183–195. https://doi.org/10.1016/j.fusengdes.2018.11.028.

[10] ANSYS Inc., ANSYS CFX Solver Modeling Guide 18.2, ANSYS, 2017.

[11] A. Tassone, G. Caruso, A. Del Nevo, I. Di Piazza, CFD simulation of the magnetohydrodynamic flow inside the WCLL breeding blanket module, Fusion Eng. Des. 124 (2017) 705–709. https://doi.org/10.1016/j.fusengdes.2017.05.098.

[12] A. Tassone, Study on liquid metal magnetohydrodynamic flows and numerical application to a water-cooled blanket for fusion reactors, Sapienza University of Rome, PhD thesis, 2019.

[13] I.R. Kirillov, C.B. Reed, L. Barleon, K. Miyazaki, Present understanding of MHD and heat transfer phenomena for liquid metal blankets, Fusion Eng. Des. 27 (1995) 553–569. https://doi.org/10.1016/0920-3796(95)90171-X.

[14] J. Reimann, G. Benamati, R. Moreau, Report of working group MHD for the blanket concept selection exercise (BSE), Karlsruhe, 1995. https://publikationen.bibliothek.kit.edu/270038027.

[15] A. Tassone, S. Siriano, G. Caruso, A. Del Nevo, MHD Pressure Drop Estimate for the WCLL In-vessel PbLi Loop, Fusion Eng. Des. (in press) (n.d.).

[16] S. Siriano, A. Tassone, G. Caruso, A. Del Nevo, Electromagnetic coupling phenomena in co-axial rectangular channels, Fusion Eng. Des. (submitted (n.d.).